UniScatter: Unifying Backscatter Communications, Symbiotic Radio and Reconfigurable Intelligent Surface

Yang Zhao, *Member, IEEE,* and Bruno Clerckx, *Fellow, IEEE*

***Abstract*—Scatterers can harvest energy from, modulate information over, and influence propagation of surrounding radio waves. Backscatter Communications (BackCom) varies object impedance to manipulate the magnitude, phase, and/or frequency of scattered signal to encode information and deliver within coverage. Reconfigurable Intelligent Surface (RIS) adapts scattering antennas or programmable metamaterial to control wireless propagation environment by boosting/suppressing signal strength in specific directions. Symbiotic Radio (SR) incorporates scatter nodes into active networks that recycle ambient signal to transmit self information and enhance legacy channel to the cooperative receiver. In this paper, we depart from those concepts and introduce UniScatter as a new paradigm for future wireless networks. Instead of treating probability distribution of reflection states as equiprobable (as scattering source of BackCom/SR) or degenerate (as reflecting element of RIS), UniScatter nodes located at different places adapt the input distribution of passive scatterers based on link priority and Channel State Information (CSI), balancing information encoding and channel reconfiguration in a flexible and mutualistic manner. To accommodate signal characteristics, UniScatter receiver semi-coherently decodes all nodes from accumulated energy, determines equivalent primary channel over reflection pattern, then coherently decodes the primary link under enhanced multipath. It reduces the complexity of cooperative decoding while preserves the benefits of backscatter modulation and passive beamforming. Using shared spectrum, energy, and infrastructures, UniScatter is a general and powerful transmit-assist protocol that unifies BackCom, RIS and SR with universal hardware design and augmented Quality of Service (QoS) control. We consider an application scenario where a multi-antenna Access Point (AP) serves a single-antenna user surrounded by multiple UniScatter nodes, and characterize the achievable primary-total-backscatter rate region by designing input distribution at the nodes, active beamforming at the AP, and backscatter decision regions at the user. Simulation results demonstrate UniScatter nodes can flexibly control the transmit-assist tradeoff via smart input distribution design.**

I. Introduction

FUTURE wireless network is envisioned to provide high throughput, uniform coverage, pervasive connectivity, heterogeneous control, and cognitive intelligence for trillions of portable devices. As an emerging low-power communication technique, Backscatter Communications (BackCom) separates conventional transmitter into a Radio-Frequency (RF) emitter with power-hungry elements (e.g., synthesizer and amplifier), and an information-bearing node with power-efficient components (e.g., harvester and modulator) [1]. The node harvests energy from emitted wave and embeds information over scattered signal in a sustainable and controllable manner. The backscatter reader can be either co-located or separated with the emitter, known as monostatic and bistatic BackCom. Its applications such as Radio-Frequency Identification (RFID) [2], [3] and passive sensor network [4], [5] have been extensively researched, standardized, and commercialized to support Internet of Things (IoT) and Machine to Machine (M2M). However, traditional BackCom requires dedicated carrier emitter and backscatter reader, while passive nodes only respond when externally inquired. In Ambient Backscatter Communications (AmBC) [6], interactive nodes recycle ambient signals generated by legacy transmitters (e.g., radio, television, and Wi-Fi) to harvest energy and establish connection in between. It eliminates the need of dedicated power source, carrier emitter, and frequency spectrum, bringing more opportunities to low-power communications. To combat the strong direct-link interference of AmBC, [7] proposed a co-located receiver that cooperatively decodes the primary (legacy) and backscatter links. The authors evaluated the error performance of Maximum-Likelihood (ML), linear, and Successive Interference Cancellation (SIC) detectors for flat fading channel, and proposed a low-complexity detector for frequency-selective fading channel. The concept of cooperative AmBC was then refined as Symbiotic Radio (SR) to cognitively incorporate AmBC with existing systems [8]. In SR, the primary transmitter generates active radio carrying primary information, the secondary node modulates scattered component with backscatter information, and the cooperative receiver decodes both links from two propagation paths. The direct transmitter-receiver path only contains primary information, while the cascaded transmitter-node-receiver path preserves both thanks to signal characteristics. Such a coexistence was further classified into commensal, parasitic, and competitive relationships based on link priority [9], and their instantaneous rates, optimal power allocations, and outage probabilities were subsequently derived in [9], [10]. However, one important issue of SR is practical cooperative decoding design. Due to physical constraints at the load-switching modulator, backscatter symbol period is typically longer than primary. Ideal joint ML decoding achieves optimal performance with prohibitive computational complexity [7], [8], [11]. For sequential decoding from primary to backscatter, [12] pointed out the randomness from backscatter modulation can be modelled as either interference or channel uncertainty, depending on the symbol period ratio. The authors concluded if this ratio is sufficiently large, the non-coherent primary achievable rate would asymptotically approach its coherent counterpart. This motivated [7]–[17] to

The authors are with the Department of Electrical and Electronic Engineering, Imperial College London, London SW7 2AZ, U.K. (e-mail: {yang.zhao18, b.clerckx}@imperial.ac.uk).

first decode the primary link, perform SIC, then decode the backscatter link. However, the advantage of SIC is questionable because 1) sufficiently large symbol period ratio is assumed in primary rate analysis and constraints backscatter rate; 2) backscatter pattern and signal characteristics are not fully exploited; 3) non-coherent primary encoding is required at the transmitter, while re-encoding, precoding, and subtraction are required at the receiver; 4) primary and backscatter symbols are superimposed by multiplication instead of superposition. Another open issue for SR is backscatter multiple access. [15] extended SIC to multi-node scenario and proposed a backscatter Non-Orthogonal Multiple Access (NOMA)-based SR with decoding order following backscatter signal strength. However, its performance deteriorates fast when the number of nodes increases. Backscatter Time-Division Multiple Access (TDMA) was also evaluated in [16], where each node transmits information during dedicated slot and harvests energy during others. It enhances energy efficiency by transmission time and reflection ratio optimization, but requires regular feedback to passive nodes and incurs high coordination cost. [18] controls the load-switching speed at nodes to shift the scattered signal to desired frequency bands. This enables backscatter Frequency-Division Multiple Access (FDMA) at the cost of extra bandwidth and higher power consumption. To reduce coordination between passive nodes, [17] proposed a random code-assisted multiple access for SR and evaluated the asymptotic Signal-to-Interference-plus-Noise Ratio (SINR) using random matrix theory. However, it suffers from imperfect synchronization and the near-far problem.

On the other hand, Reconfigurable Intelligent Surface (RIS) is a promising technology that evolves wireless propagation environment using numerous passive reflecting elements (e.g., scattering antenna or programmable metamaterial) with adjustable amplitudes and/or phases [19]. The scattered signals contain no additional information, but adds constructively or destructively with the direct component to enhance desired signal or suppress interference. Compared with backscatter nodes of BackCom/SR, RIS elements employ deterministic reflection pattern priorly known at transmitter and receiver. This motivated the use of fixed reflection coefficients during each channel block to improve communication, sensing, and power performances [20]–[25]. The concept of dynamic RIS, namely choosing independent reflection coefficients over different time slots within channel block, was first considered for resource blocks of Orthogonal Frequency-Division Multiplexing (OFDM) systems, then extended to power and information phases of Wireless Powered Communication Network (WPCN) [26]–[28]. Dynamic RIS provides artificial channel diversity and flexible resource allocation, but misses the opportunity to encode its own message. From an information-theoretic perspective, [29] reported using RIS as an auxiliary passive beamforming device to maximize the Signal-to-Noise Ratio (SNR) is generally rate-suboptimal for finite input constellations. Instead, joint transmitter-RIS encoding achieves the capacity of RIS-aided channel, and layered encoding with SIC decoding (i.e., SIC-based SR) can outperform pure passive beamforming at high SNR. It inspired [30]–[39] to employ RIS also as an information source to combine passive beamforming and backscatter modulation in the overall reflection pattern. In particular, *symbol level precoding* maps backscatter symbols to RIS coefficient sets optimized for detection [30], [31], *overlay modulation* superposes information-bearing symbols over a common auxiliary matrix [32]–[35], *spatial modulation* switches between reflection coefficient sets that maximize SNR at different receive antennas [36]–[38], and *index modulation* divides RIS into reflection elements for passive beamforming and information elements for on-off modulation [39]. However, those RIS-empowered BackCom/SR designs involve advanced hardware architecture, high optimization complexity, and additional control overhead.

To the best of our knowledge, all relevant literatures assumed at backscatter information sources either Gaussian codebook [9], [10], [12]–[16], [34] or finite equiprobable inputs [7], [8], [11], [17], [30]–[33], [35]–[39]. The former is impractical for passive backscatter devices, while the latter does not fully exploit reflection pattern and Channel State Information (CSI). In this paper, we introduce UniScatter that generalizes BackCom, SR, and RIS to manipulate the transmit-assist tradeoff via smart input distribution and backscatter detector design. The contributions of this paper are summarized as follows.

First, we propose UniScatter nodes to adapt the input probability distribution of a finite-state passive scatter device based on link priority and CSI. The reflection pattern over time is no longer fully random or deterministic, but can be flexibly distributed to unify and balance backscatter modulation with passive beamforming. Scattering source of BackCom/SR and reflecting element of RIS can be regarded as its extreme cases, where the input distribution boils down to equiprobable and degenerate, respectively. Like aforementioned RIS-empowered BackCom/SR schemes, the passive nodes require regular coordination with active devices, but the advantages are 1) UniScatter nodes can be built over conventional load-switching scatterers instead of composite metamaterial; 2) the optimization cost of input distribution is much lower than that of RIS reflection coefficients; 3) adaptive backscatter channel coding can exploit CSI to achieve higher instantaneous rate than conventional uncoded transmission; 4) the physically distributed characteristics of UniScatter nodes and legacy users avoids the development optimization and allows uniformly good performance for both links.

Second, we propose a practical UniScatter receiver that semi-coherently decodes UniScatter nodes from the received energy per backscatter block, re-encodes for their reflection patterns, retrieves equivalent primary channel as if dynamic passive beamforming, then coherently decodes the primary link under the enhanced multipath. The proposed receiver 1) preserves the benefits of backscatter modulation and passive beamforming; 2) enjoys lower computational and operational complexities than joint ML and SIC schemes; 3) accommodates the link difference and suits for diverse symbol period ratios; 4) requires minor modification over legacy hardware.

Third, we consider an application scenario where multiple UniScatter nodes ride over a point-to-point Multiple-Input Single-Output (MISO) transmission, performing backscatter modulation and passive beamforming to a nearby user using shared spectrum, energy, and infrastructures. To investigate how UniScatter unifies BackCom, SR and RIS for the benefits of both coexisting subsystems, we provide primary and backscatter rate analyses and emphasize the contributions of input distribution at UniScatter nodes, active beamforming at the Access Point (AP), and backscatter decision regions at the user. This is the first paper to reveal the importance of those factors in RIS-empowered BackCom/SR.

Fourth, we characterize the achievable primary-total-backscatter rate region of the aforementioned system by optimizing the input distribution, active beamforming, and backscatter decision regions. It is formulated as a weighted sum-rate maximization subject to input probability simplex, average transmit power, and sequential decision threshold constraints. Since the original problem is highly non-convex, we decouple it into individual subproblems and constraint all decision regions to convex (connected) intervals. A suboptimal Block Coordinate Descent (BCD) algorithm is then proposed, where the Karush-Kuhn-Tucker (KKT) input distribution is numerically evaluated by limit of sequences, the active beamforming is iteratively updated by Projected Gradient Descent (PGD) accelerated by backtracking line search, and the decision regions are refined by existing thresholding designs.

Fifth, we provide numerical results to demonstrate the benefits of UniScatter and proposed algorithms. It is concluded that 1) UniScatter nodes provide flexible transmit-assist tradeoff using adaptive input distribution design; 2) when primary link is absolutely prioritized, the input probability of each node is 1 at one state and 0 at the others, which coincides with discretized RIS; 3) when backscatter link is absolutely prioritized, UniScatter nodes can exploit adaptive channel coding to achieve higher instantaneous rate than uncoded equiprobable inputs of BackCom/SR; 4) the proposed KKT input distribution design converges to stationary points, whose average performance is very close to global optimal; 5) the PGD beamforming achieves larger rate region than conventional Maximum Ratio Transmission (MRT); 6) the decision region schemes adapted to input distribution provide higher backscatter rates than the non-adaptive ML detector; 7) cooperation between passive nodes in terms of joint encoding can further boost the total backscatter rate; 8) the low complexity of input distribution design and the marginal effect of increasing reflection states motivates the use of low-order scatter nodes to replace high-resolution RIS.

Notations: Italic, bold lower-case, and bold upper-case letters denote scalars, vectors and matrices, respectively. $\mathbf{0}$ and $\mathbf{1}$ denote zero and one array of appropriate size, respectively. $\mathbb{I}^{x\times y}$, $\mathbb{R}_+^{x\times y}$, and $\mathbb{C}^{x\times y}$ denote the unit, real nonnegative, and complex spaces of dimension $x\times y$, respectively. j denotes the imaginary unit. $\mathrm{diag}(\cdot)$ returns a square matrix with the input vector on its main diagonal and zeros elsewhere. $\mathrm{card}(\cdot)$ returns the cardinality of a set. $(\cdot)^*$, $(\cdot)^T$, $(\cdot)^H$, $|\cdot|$, and $\|\cdot\|$ denote the conjugate, transpose, conjugate transpose, absolute value, and Euclidean norm operators, respectively. $(\cdot)^{(r)}$ and $(\cdot)^\star$ denote the r-th iterated and terminal solutions, respectively. The distribution of a Circularly Symmetric Complex Gaussian (CSCG) random variable with zero mean and variance σ^2 is denoted by $\mathcal{CN}(0,\sigma^2)$, and $\sim$ means "distributed as".

II. Scattering Principles

Scattering refers to a change of moving direction of particles after colliding with others. It often involves *diffuse reflection* where an incident ray is redistributed at many angles. An electromagnetic wave is scattered when an obstruction is placed in its propagation path. In this section, we first introduce two common scatterer categories and review their operation principles, then briefly discuss how scatterers realize backscatter modulation and channel reconfiguration over reflection patterns.

A. Scatterer Categories

In RF applications such as BackCom, SR and RIS, the scatterer often includes *variable-load antenna* or *programmable metamaterial* with various reflection patterns [40].

1) Antenna-Based Scatterer: A typical antenna-based scatterer consists of an integrated antenna, a load-switching modulator, an energy harvester, and on-chip components (e.g., microcontroller and sensors) [2]. It first receives the impinging signals, then reradiates some back to the space and dissipates the remainder. According to transmission line theory, the scatter-absorb tradeoff depends on the impedance matching of the load and the antenna. For passive scatterers without dedicated energy source, a majority of incident wave is harvested to support node operation and the reradiated part can be relatively weak [41]. At the receiver, the observed signal can be further decomposed into *structural mode* and *antenna mode* components [42]. The former consistently contributes to environment multipath and is modelled within channel estimation, while the latter depends on impedance mismatch and can be used for backscatter modulation [1] and/or channel reconfiguration [40]. For antenna-based scatterers, the reflection coefficient at load state m is[1]

$$\mathit{\Gamma}_m = \frac{Z_m - Z_{\mathrm{A}}^*}{Z_m + Z_{\mathrm{A}}}, \tag{1}$$

where Z_m is the load impedance at state m and Z_{A} is the antenna input impedance.

2) Metamaterial-Based Scatterer: A typical metamaterial-based scatterer consists of multiple material layers and a smart controller [43]. The outer metamaterial layer involves numerous sub-wavelength structural units made of metallic or dielectric materials. The properties of unit cells can be artificially tuned for unconventional effective permittivity ϵ and permeability μ, producing customizable response to the electromagnetic field [44]. Using epsilon-negative material (e.g., conducing rods) or mu-negative material (e.g., split-ring resonators), ideal metamaterial-based scatterers can reflect the incident waves at the boundary between free space and metamaterial without receiving them [45]. This mainly applies a phase shift on the reflected wave and any propagation into the metamaterial would be evanescent. Depending on the type of metamaterial, its equivalent impedance can be controlled by voltage (for functional materials [46] and tunable diodes [47]) or architecture (for resonant elements [48]). For metamaterial-based scatterers with a discrete impedance set, the reflection coefficient at metamaterial state m is

$$\mathit{\Gamma}_m = \frac{Z_m - Z_0}{Z_m + Z_0}, \tag{2}$$

[1] It corresponds to a linear scatter model where the reflection coefficient is irrelevant to incident electromagnetic field strength.

where Z_m is the equivalent impedance of metamaterial unit at state m and $Z_0 = 377\Omega$ is the characteristic impedance of free space.

B. BackCom/SR: Backscatter Modulation

BackCom and SR commonly employ antenna-based scatterers as passive information sources. By *frequently switching* between the available states, each backscatter node encodes self message over scattered signal and introduces backscatter uncertainty at the receiver. For M-ary Quadrature Amplitude Modulation (QAM), reflection coefficient $\mathit{\Gamma}_m$ maps to the corresponding *complex constellation point* c_m by

$$\mathit{\Gamma}_m = \alpha \frac{c_m}{\max_{m'} |c_{m'}|}, \tag{3}$$

where $\alpha \in \mathbb{I}$ is the amplitude scattering ratio at the direction of interest.

C. RIS: Channel Reconfiguration

RIS typically involves a planar antenna array or metasurface of numerous metamaterial units as a passive channel reconfigurator. By *adaptively choosing* the reflection pattern, each reflecting element alters the phase of scattered signal for constructive/destructive superposition at the receiver. For each unit with M candidate states, reflection coefficient $\mathit{\Gamma}_m$ maps to the corresponding *phase shift* θ_m by

$$\mathit{\Gamma}_m = \beta_m \exp(j\theta_m), \tag{4}$$

where $\beta_m \in \mathbb{I}$ is the overall amplitude scattering ratio of state m.

D. Opportunities

We have seen conventional scattering applications as BackCom, SR and RIS using the reflection pattern (1), (2) for either backscatter modulation (3) or passive beamforming (4). A natural but critical question is, for a given scatterer with pre-determined reflection pattern set, *can we softly bridge backscatter modulation and passive beamforming by appropriate reflection design?* This question is answered in Section III.

III. UniScatter

Using shared spectrum, energy and infrastructures, UniScatter is a novel passive communication/assistance protocol that generalizes BackCom, SR and RIS in a *physically* and *probabilistically* distributed manner. In particular, passive UniScatter nodes located at different places ride over an active legacy transmission in a flexible and mutualistic manner, while practical UniScatter receiver cooperatively decodes both primary and backscatter links under the benefits of backscatter modulation and passive beamforming.

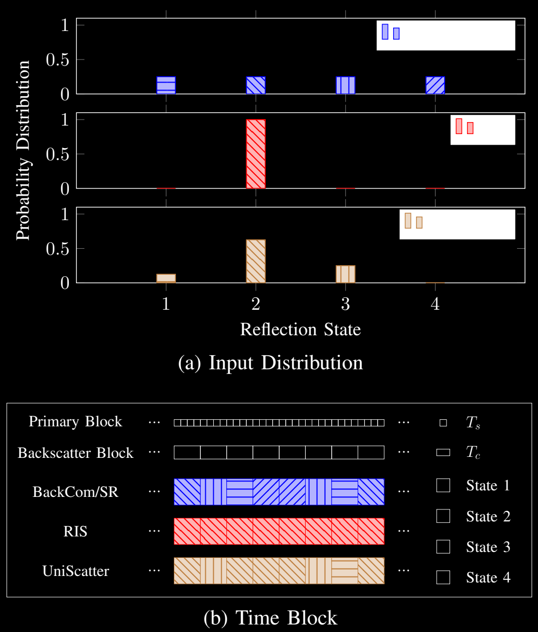

Fig. 1. Input probability distribution and time block structure of BackCom, SR, RIS, and UniScatter. T_s and T_c respectively denote the primary and backscatter symbol period. Within channel coherence time, UniScatter nodes semi-randomly select reflection state for each backscatter symbol block under the guidance of input probability distribution.

A. UniScatter Nodes

Based on link priority and CSI, UniScatter nodes adapt the *state input probability distribution* of antenna-based scatterers to unify backscatter modulation and passive beamforming. The scattering sources of BackCom/SR and reflecting elements of RIS can be viewed as its extreme cases, where the input distribution boils down to equiprobable and degenerate, respectively. As illustrated in Fig. 1, instead of always using fully random or deterministic reflection pattern over time, each UniScatter node can *flexibly adjust* its input distribution to balance information encoding and channel reconfiguration. That is, it semi-randomly select the reflection state per backscatter symbol block under the guidance of input probability $P(\mathit{\Gamma}_m)$ for state m. Such an adaptive backscatter channel coding coincides with RIS when primary link is absolutely prioritized, and outperforms the uncoded equiprobable inputs of BackCom/SR when backscatter link is absolutely prioritized. Besides, the physically distributed characteristics of UniScatter nodes and legacy users avoids the development optimization and allows uniformly good performance for both links.

As shown in Fig. 2(a), UniScatter nodes can be implemented over readily available passive backscatter devices with energy harvester and information decoder. Its equivalent circuit and scatter model are presented in Fig. 2(b) and 2(c). When activated by primary transmitter, each node harvests a proportion of the impinging wave for its own operation, decode the embedded coordination information for input distribution control, then applies a potentially random phase shift on the reradiated signal due to backscatter modulation. Energy harvesting and information decoding at passive UniScatter nodes can be realized using conventional power-splitting or time-sharing Simultaneous Wireless Information and Power Transfer

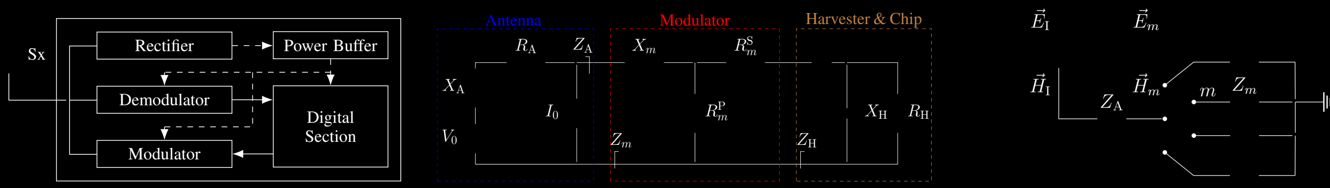

(a) Block Diagram (b) Equivalent Circuit (c) Scatter Model

Fig. 2. Block diagram, equivalent circuit, and scatter model of a UniScatter node. The solid and dashed vectors represent signal and energy flows. The scattering antenna behaves as a constant power source, where the voltage V_0 and current I_0 are introduced by incident electric field $\vec{E}_{\mathrm{I}}$ and magnetic field $\vec{H}_{\mathrm{I}}$ [55].

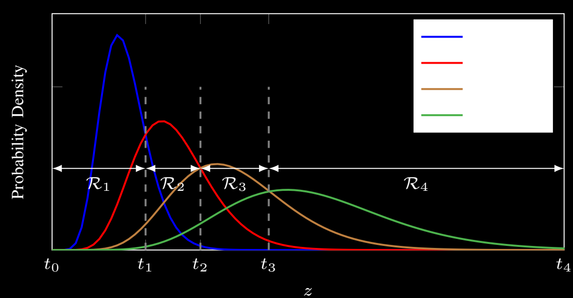

Fig. 3. PDF of total received energy per backscatter block, conditioned on different input state hypotheses. t and $\mathcal{R}$ denote the energy decision thresholds and regions, respectively.

(SWIPT) protocols [49] or integrated energy-information receiver with pulse position modulated signal [50]. Besides, relevant CSI can be acquired using either traditional sequential methods [51]–[53] or the state-of-the-art parallel approach [54]. In the following context, we assume perfect primary-backscatter coordination and perfect channel estimation for all links.

B. UniScatter Receiver

Since each passive UniScatter node directly modulates its own message over the legacy signal, it involves a *double modulation* where the primary and backscatter symbols are superimposed by *multiplication coding* instead of superposition coding. Besides, the backscatter symbol period is typically longer than primary due to the load switching speed constraint. Those facts imply *backscatter detection* under primary uncertainty can be viewed as part of *primary channel training*. Hence, we propose a practical UniScatter receiver that semi-coherently decodes UniScatter nodes from the received energy per backscatter block, re-encodes for their reflection patterns, retrieves equivalent primary channel as if dynamic passive beamforming, then coherently decodes the primary link under the enhanced multipath. As illustrated in Fig. 3, the total received energy per backscatter block is a random variable that follows different distributions conditioned on different input state hypotheses. Compared with conventional joint ML and SIC from stronger primary link to weaker backscatter links, UniScatter receiver not only preserves the benefits of backscatter modulation and passive beamforming, but also enjoys much lower computational and operational complexities.

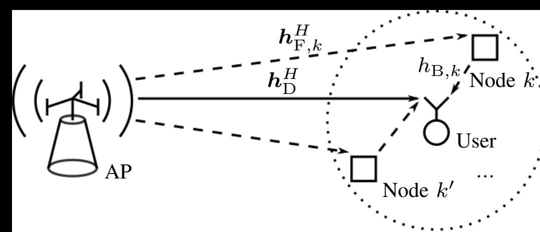

Fig. 4. A single-user multi-node UniScatter system.

C. System Model

To demonstrate the advantages of UniScatter, we consider a single-user multi-node MISO UniScatter system as shown in Fig. 4. In the primary active point-to-point system, a Q-antenna AP transmits to a single-antenna user assisted by K nearby single-antenna UniScatter nodes with M reflection states. In the secondary backscatter Multiple Access Channel (MAC) system, the AP serves as the carrier emitter, the distributed UniScatter nodes modulate information over reradiated RF signals, and the user decodes their messages. For simplicity, we consider a quasi-static block fading model where channels remain constant within coherence block and vary independently between consecutive blocks. Due to the physical constraints of load switching speed, we assume the backscatter over primary symbol period ratio is an integer $N \gg 1$. We also omit the signal reflected by two or more times and ignore the propagation time difference of different paths.

Denote the AP-user direct channel as $\boldsymbol{h}_{\mathrm{D}}^H \in \mathbb{C}^{1\times Q}$, the AP-node $k \in \mathcal{K} \triangleq \{1,\dots,K\}$ forward channel as $\boldsymbol{h}_{\mathrm{F},k}^H \in \mathbb{C}^{1\times Q}$, the node k-user backward channel as $h_{\mathrm{B},k}$, and the cascaded channel via tag k as $\boldsymbol{h}_{\mathrm{C},k}^H \triangleq h_{\mathrm{B},k}\boldsymbol{h}_{\mathrm{F},k}^H \in \mathbb{C}^{1\times Q}$. Let $x_{\mathcal{K}} \triangleq (x_1, \dots, x_K)$ be the backscatter symbol tuple of all UniScatter nodes. Without loss of generality, we consider one specific backscatter block (i.e., N primary blocks) in the following context. Due to double modulation, the equivalent primary channel is a function of *coded* backscatter symbols

$$\boldsymbol{h}_{\mathrm{E}}^H(x_{\mathcal{K}}) \triangleq \boldsymbol{h}_{\mathrm{D}}^H + \sum_{k\in\mathcal{K}} \alpha_k \boldsymbol{h}_{\mathrm{C},k}^H x_k = \boldsymbol{h}_{\mathrm{D}}^H + \boldsymbol{x}^H \operatorname{diag}(\boldsymbol{\alpha})\boldsymbol{H}_{\mathrm{C}}, \quad (5)$$

where $\alpha_k \in \mathbb{I}$ is the amplitude scattering ratio of UniScatter node k, $x_k \in \mathcal{X} \triangleq \{c_1,\dots,c_M\}$ is the *coded* backscatter symbol of node k, $\boldsymbol{\alpha} \triangleq [\alpha_1,\dots,\alpha_K]^T \in \mathbb{I}^K$, $\boldsymbol{x} \triangleq [x_1,\dots,x_K]^H \in \mathcal{X}^K$, and $\boldsymbol{H}_{\mathrm{C}} \triangleq [\boldsymbol{h}_{\mathrm{C},1},\dots,\boldsymbol{h}_{\mathrm{C},K}]^H \in \mathbb{C}^{K\times Q}$. The signal received by the user at primary block $n \in \mathcal{N} \triangleq \{1,\dots,N\}$ is

$$y[n] = \boldsymbol{h}_{\mathrm{E}}^H(x_{\mathcal{K}})\boldsymbol{w}s[n] + v[n], \quad (6)$$

where $s \sim \mathcal{CN}(0,1)$ is the primary symbol, $v \sim \mathcal{CN}(0,\sigma_v^2)$ is the Additive White Gaussian Noise (AWGN), and $\boldsymbol{w} \in \mathbb{C}^Q$ is the active beamforming vector subject to average transmit power constraint $\|\boldsymbol{w}\|^2 \leq P$. Denote $m_k \in \mathcal{M} \triangleq \{1,...,M\}$ as the reflection state index of node k, and $m_{\mathcal{K}} \triangleq (m_1,...,m_K)$ as the state index tuple of all nodes. Conditioned on backscatter index tuple $m_{\mathcal{K}}$, the received signal (6) follows CSCG distribution $y[n] \sim \mathcal{CN}(0,\sigma_{m_{\mathcal{K}}}^2)$, where

$$\sigma_{m_{\mathcal{K}}}^2 = |\boldsymbol{h}_{\mathrm{E}}^H(x_{m_{\mathcal{K}}})\boldsymbol{w}|^2 + \sigma_v^2 \tag{7}$$

is the received variance and $x_{m_{\mathcal{K}}}$ is the backscatter symbol tuple associated with $m_{\mathcal{K}}$. For node k, let x_{m_k} be the backscatter symbol associated with index m_k.[2] Besides, we define the total received energy per backscatter block as $z = \sum_{n=1}^N |y[n]|^2$. Since z is the sum of N independent and identically distributed (i.i.d.) exponential variables, its PDF conditioned on $m_{\mathcal{K}}$ follows Gamma distribution

$$f(z|\mathcal{H}_{m_{\mathcal{K}}}) = \frac{z^{N-1}\exp(-z/\sigma_{m_{\mathcal{K}}}^2)}{\sigma_{m_{\mathcal{K}}}^{2N}(N-1)!}, \tag{8}$$

where $\mathcal{H}_{m_{\mathcal{K}}}$ denotes hypothesis $m_{\mathcal{K}}$. As illustrated in Fig. 3, the UniScatter receiver divides the received energy space into disjoint decision regions associated with those hypotheses. For example, if the total received energy during a backscatter block falls within region $\mathcal{R}_{m_{\mathcal{K}}}$, then the detector output would be $x_{m_{\mathcal{K}}}$.

Remark 1. *Interestingly, the capacity-achieving decision design for Discrete Memoryless Thresholding Channel (DMTC) remains under-investigated, and some attempts were made for a single source with binary inputs [56], [57]. For non-binary inputs with arbitrary distribution, the optimal decision region for each letter can be non-convex (i.e., with non-adjacent partitions) and the optimal number of thresholds is still unknown [58], [59].*

Like most existing literatures, we limit the scope of this paper to convex decision regions and consider sequential decision thresholds design therein. For the ease of notations, we define a general bijective function from backscatter index tuple $m_{\mathcal{K}}$ to integer $l \in \mathcal{L} \triangleq \{1,...,L \triangleq M^K\}$, where $\{\sigma_l^2\}_{l \in \mathcal{L}}$ are sorted in an ascending order. Both notations are used interchangeably in the following context. As such, the convex decision region of backscatter tuple l can be written as

$$\mathcal{R}_l \triangleq [t_{l-1}, t_l), \quad t_{l-1} \leq t_l. \tag{9}$$

Once the decision threshold vector $\boldsymbol{t} \triangleq [t_0,...,t_L]^T \in \mathbb{R}_+^{(L+1)}$ is determined, we can formulate a Discrete Memoryless Thresholding Multiple Access Channel (DMTMAC) with transition probability from input $x_{m_{\mathcal{K}}}$ to output $\hat{x}_{m'_{\mathcal{K}}}$

$$P(\hat{x}_{m'_{\mathcal{K}}}|x_{m_{\mathcal{K}}}) = \int_{\mathcal{R}_{m'_{\mathcal{K}}}} f(z|\mathcal{H}_{m_{\mathcal{K}}})dz, \tag{10}$$

then perform backscatter channel coding on top of it.

[2]Please note x_k and $x_{\mathcal{K}}$ are random variable and tuple, while x_{m_k} and $x_{m_{\mathcal{K}}}$ are their instances of index m_k and $m_{\mathcal{K}}$.

D. Information Theory

Denote the input probability distribution vector of node k as $\boldsymbol{p}_k \triangleq [P_k(c_1),...,P_k(c_M)]^T \in \mathbb{I}^M$, and the probability of state m_k as $P_k(x_{m_k})$. With independent encoding at all nodes, the probability of backscatter symbol tuple $x_{m_{\mathcal{K}}}$ is

$$P_{\mathcal{K}}(x_{m_{\mathcal{K}}}) = \prod_{k \in \mathcal{K}} P_k(x_{m_k}). \tag{11}$$

Similar to [60], we define the backscatter information function between input symbol tuple instance $x_{m_{\mathcal{K}}}$ and output symbol tuple variable $\hat{x}_{\mathcal{K}}$ as

$$I_{\mathrm{B}}(x_{m_{\mathcal{K}}};\hat{x}_{\mathcal{K}}) \triangleq \sum_{m'_{\mathcal{K}}} P(\hat{x}_{m'_{\mathcal{K}}}|x_{m_{\mathcal{K}}}) \log \frac{P(\hat{x}_{m'_{\mathcal{K}}}|x_{m_{\mathcal{K}}})}{P_{\mathcal{K}}(\hat{x}_{m'_{\mathcal{K}}})}, \tag{12}$$

where $P_{\mathcal{K}}(\hat{x}_{m'_{\mathcal{K}}}) = \sum_{m_{\mathcal{K}}} P_{\mathcal{K}}(x_{m_{\mathcal{K}}}) P(\hat{x}_{m'_{\mathcal{K}}}|x_{m_{\mathcal{K}}})$ is the probability of channel output tuple $\hat{x}_{m'_{\mathcal{K}}}$. We also define the backscatter marginal information of letter x_{m_k} of node k as

$$I_{\mathrm{B},k}(x_{m_k};\hat{x}_{\mathcal{K}}) \triangleq \sum_{m_{\mathcal{K}\setminus\{k\}}} P_{\mathcal{K}\setminus\{k\}}(x_{m_{\mathcal{K}\setminus\{k\}}}) I_{\mathrm{B}}(x_{m_{\mathcal{K}}};\hat{x}_{\mathcal{K}}), \tag{13}$$

where $P_{\mathcal{K}\setminus\{k\}}(x_{m_{\mathcal{K}\setminus\{k\}}}) = \prod_{q \in \mathcal{K}\setminus\{k\}} P_q(x_{m_q})$. The backscatter mutual information can be written as

$$I_{\mathrm{B}}(x_{\mathcal{K}};\hat{x}_{\mathcal{K}}) = \sum_{m_{\mathcal{K}}} P_{\mathcal{K}}(x_{m_{\mathcal{K}}}) I_{\mathrm{B}}(x_{m_{\mathcal{K}}};\hat{x}_{\mathcal{K}}). \tag{14}$$

Once backscatter messages of all nodes are successfully decoded, we can re-code for backscatter symbol tuple $x_{\mathcal{K}}$, recover their reflection patterns by (3), and retrieve the equivalent primary channel by (5). Moreover, we define the primary information function conditioned on backscatter symbol tuple $x_{m_{\mathcal{K}}}$ as

$$I_{\mathrm{P}}(s;y|x_{m_{\mathcal{K}}}) \triangleq \log\left(1 + \frac{|\boldsymbol{h}_{\mathrm{E}}^H(x_{m_{\mathcal{K}}})\boldsymbol{w}|^2}{\sigma_v^2}\right), \tag{15}$$

the primary marginal information conditioned on letter x_{m_k} of node k as

$$I_{\mathrm{P},k}(s;y|x_{m_k}) \triangleq \sum_{m_{\mathcal{K}\setminus\{k\}}} P_{\mathcal{K}\setminus\{k\}}(x_{m_{\mathcal{K}\setminus\{k\}}}) I_{\mathrm{P}}(s;y|x_{m_{\mathcal{K}}}), \tag{16}$$

and the primary ergodic mutual information as

$$I_{\mathrm{P}}(s;y|x_{\mathcal{K}}) = \sum_{m_{\mathcal{K}}} P_{\mathcal{K}}(x_{m_{\mathcal{K}}}) I_{\mathrm{P}}(s;y|x_{m_{\mathcal{K}}}). \tag{17}$$

With a slight abuse of notation, we define the corresponding weighted sum information function, marginal information, and mutual information respectively as

$$I(x_{m_{\mathcal{K}}}) \triangleq \rho I_{\mathrm{P}}(s;y|x_{m_{\mathcal{K}}}) + (1-\rho) I_{\mathrm{B}}(x_{m_{\mathcal{K}}};\hat{x}_{\mathcal{K}}), \tag{18}$$

$$I_k(x_{m_k}) \triangleq \rho I_{\mathrm{P},k}(s;y|x_{m_k}) + (1-\rho) I_{\mathrm{B},k}(x_{m_k};\hat{x}_{\mathcal{K}}), \tag{19}$$

$$I(x_{\mathcal{K}}) \triangleq \rho I_{\mathrm{P}}(s;y|x_{\mathcal{K}}) + (1-\rho) I_{\mathrm{B}}(x_{\mathcal{K}};\hat{x}_{\mathcal{K}}), \tag{20}$$

where $\rho \in \mathbb{I}$ is the relative priority of the primary link.

IV. Rate-Region Characterization

To characterize the achievable primary-total-backscatter rate region of the proposed UniScatter system, we aim to maximize the weighted sum mutual information with respect to input distribution $\{\boldsymbol{p}_k\}_{k\in\mathcal{K}}$, active beamforming $\boldsymbol{w}$, and decision thresholds $\boldsymbol{t}$ as

$$\begin{aligned}
\max_{\{\boldsymbol{p}_k\}_{k\in\mathcal{K}},\boldsymbol{w},\boldsymbol{t}} \quad & I(x_{\mathcal{K}}) && \text{(21a)}\\
\text{s.t.} \quad & \mathbf{1}^T\boldsymbol{p}_k = 1, \quad \forall k, && \text{(21b)}\\
& \boldsymbol{p}_k \geq \mathbf{0}, \quad \forall k, && \text{(21c)}\\
& \|\boldsymbol{w}\|^2 \leq P, && \text{(21d)}\\
& \boldsymbol{t} \geq \mathbf{0}. && \text{(21e)}
\end{aligned}$$

Since problem (21) is highly non-convex, we propose a BCD algorithm that iteratively updates $\{\boldsymbol{p}_k\}_{k\in\mathcal{K}}$, $\boldsymbol{w}$ and $\boldsymbol{t}$ until convergence.

A. Input Distribution

For any given $\boldsymbol{w}$ and $\boldsymbol{t}$, we can construct the equivalent DMTMAC by (10) and simplify (21) to

$$\begin{aligned}
\max_{\{\boldsymbol{p}_k\}_{k\in\mathcal{K}}} \quad & I(x_{\mathcal{K}}) && \text{(22a)}\\
\text{s.t.} \quad & \text{(21b),(21c)}, && \text{(22b)}
\end{aligned}$$

which involves the coupled term $\prod_{k\in\mathcal{K}} P_k(x_{m_k})$ and is non-convex when $K>1$. Following [60], we first recast KKT conditions of problem (22) to their equivalent forms, then propose a numerical method that guarantees those conditions on convergence of sequences.

Remark 2. *As demonstrated in [61], KKT conditions are generally necessary but insufficient for total rate maximization problems. Although KKT solutions to problem* (22) *may end up being saddle points, we will later show by simulation their average performance can be reasonably close to optimal for a moderate K.*

Proposition 1. *The KKT optimality conditions for problem* (22) *are equivalent to, $\forall k, m_k$,*

$$\begin{aligned}
I_k^\star(x_{m_k}) &= I^\star(x_{\mathcal{K}}), \quad P_k^\star(x_{m_k}) > 0, && \text{(23a)}\\
I_k^\star(x_{m_k}) &\leq I^\star(x_{\mathcal{K}}), \quad P_k^\star(x_{m_k}) = 0. && \text{(23b)}
\end{aligned}$$

Proof. Please refer to Appendix A. □

For each node, (23a) suggests each probable state should produce the same marginal information (averaged over all states of other nodes), while (23b) suggests any state with potentially less marginal information should not be used.

Proposition 2. *For any strictly positive initializer $\{\boldsymbol{p}_k^{(0)}\}_{k\in\mathcal{K}}$, the KKT input probability of node k at state m_k is given by the converging point of the sequence*

$$P_k^{(r+1)}(x_{m_k}) = \frac{P_k^{(r)}(x_{m_k})\exp\Big(\frac{\rho}{1-\rho}I_k^{(r)}(x_{m_k})\Big)}{\sum_{m_k'} P_k^{(r)}(x_{m_k'})\exp\Big(\frac{\rho}{1-\rho}I_k^{(r)}(x_{m_k'})\Big)}, \quad (24)$$

where r is the iteration index.

Algorithm 1: Numerical KKT Input Distribution Evaluation by Limits of Sequence

---

Input: K, N, $\boldsymbol{h}_{\mathrm{D}}^H$, $\boldsymbol{H}_{\mathrm{C}}$, $\boldsymbol{\alpha}$, $\mathcal{X}$, σ_v^2, ρ, $\boldsymbol{w}$, $\boldsymbol{t}$, ϵ
Output: $\{\boldsymbol{p}_k^\star\}_{k\in\mathcal{K}}$
1: Set $\boldsymbol{h}_{\mathrm{E}}^H(x_{m_{\mathcal{K}}})$, $\forall m_{\mathcal{K}}$ by (5)
2: $\quad\sigma_{m_{\mathcal{K}}}^2$, $\forall m_{\mathcal{K}}$ by (7)
3: $\quad f(z|\mathcal{H}_{m_{\mathcal{K}}})$, $\forall m_{\mathcal{K}}$ by (8)
4: $\quad P(\hat{x}_{m_{\mathcal{K}}'}|x_{m_{\mathcal{K}}})$, $\forall m_{\mathcal{K}}, m_{\mathcal{K}}'$ by (10)
5: Initialize $r \leftarrow 0$
6: $\quad\quad \boldsymbol{p}_k^{(0)} > \mathbf{0}$, $\forall k$
7: Get $P_{\mathcal{K}}^{(r)}(x_{m_{\mathcal{K}}})$, $\forall m_{\mathcal{K}}$ by (11)
8: $\quad I^{(r)}(x_{m_{\mathcal{K}}})$, $\forall m_{\mathcal{K}}$ by (12), (15), (18)
9: $\quad I_k^{(r)}(x_{m_k})$, $\forall k, m_k$ by (13), (16), (19)
10: $\quad I^{(r)}(x_{\mathcal{K}})$ by (14), (17), (20)
11: **Repeat**
12: $\quad$ Update $r \leftarrow r+1$
13: $\quad\quad \boldsymbol{p}_k^{(r)}$, $\forall k$ by (24)
14: $\quad$ Redo step 7–10
15: **Until** $I^{(r)}(x_{\mathcal{K}}) - I^{(r-1)}(x_{\mathcal{K}}) \leq \epsilon$

Proof. Please refer to Appendix B. □

For (24) at iteration $r+1$, the input distribution of node k is updated over $\big\{\{\boldsymbol{p}_q^{(r+1)}\}_{q=1}^{k-1}, \{\boldsymbol{p}_q^{(r)}\}_{q=k}^{K}\big\}$. The KKT input distribution design is summarized in Algorithm 1.

B. Active Beamforming

For any given $\{\boldsymbol{p}_k\}_{k\in\mathcal{K}}$ and $\boldsymbol{t}$, problem (21) reduces to

$$\begin{aligned}
\max_{\boldsymbol{w}} \quad & I(x_{\mathcal{K}}) && \text{(25a)}\\
\text{s.t.} \quad & \text{(21d)}, && \text{(25b)}
\end{aligned}$$

which is still non-convex due to the integration and entropy terms. To tackle this, we rewrite the DMTMAC transition probability (10) from input index tuple $m_{\mathcal{K}}$ to output index l as a regularized incomplete Gamma function in the series representation [62, Theorem 3]

$$\begin{aligned}
Q\Big(N, \frac{t_{l-1}}{\sigma_{m_{\mathcal{K}}}^2}, \frac{t_l}{\sigma_{m_{\mathcal{K}}}^2}\Big) &= \frac{\int_{t_{l-1}/\sigma_{m_{\mathcal{K}}}^2}^{t_l/\sigma_{m_{\mathcal{K}}}^2} z^{N-1}\exp(-z)dz}{(N-1)!}\\
&= \exp\Big(-\frac{t_{l-1}}{\sigma_{m_{\mathcal{K}}}^2}\Big)\sum_{n=0}^{N-1}\frac{\Big(\frac{t_{l-1}}{\sigma_{m_{\mathcal{K}}}^2}\Big)^n}{n!} - \exp\Big(-\frac{t_l}{\sigma_{m_{\mathcal{K}}}^2}\Big)\sum_{n=0}^{N-1}\frac{\Big(\frac{t_l}{\sigma_{m_{\mathcal{K}}}^2}\Big)^n}{n!}.
\end{aligned} \quad (26)$$

Its gradient with respect to $\boldsymbol{w}^*$ can be derived as

$$\nabla_{\boldsymbol{w}^*} Q\Big(N, \frac{t_{l-1}}{\sigma_{m_{\mathcal{K}}}^2}, \frac{t_l}{\sigma_{m_{\mathcal{K}}}^2}\Big) = \frac{\boldsymbol{h}_{\mathrm{E}}(x_{m_{\mathcal{K}}})\boldsymbol{h}_{\mathrm{E}}^H(x_{m_{\mathcal{K}}})\boldsymbol{w}}{(\sigma_{m_{\mathcal{K}}}^2)^2} g_{m_{\mathcal{K}}}(t_{l-1}, t_l), \quad (27)$$

where $g_{m_{\mathcal{K}}}(t_{l-1}, t_l) \triangleq g_{m_{\mathcal{K}}}(t_l) - g_{m_{\mathcal{K}}}(t_{l-1})$ and

$$g_{m_{\mathcal{K}}}(t_l) = t_l \exp\Big(-\frac{t_l}{\sigma_{m_{\mathcal{K}}}^2}\Big)\Bigg(-1 + \sum_{n=1}^{N-1}\frac{\Big(n - \frac{t_l}{\sigma_{m_{\mathcal{K}}}^2}\Big)\Big(\frac{t_l}{\sigma_{m_{\mathcal{K}}}^2}\Big)^{n-1}}{n!}\Bigg). \quad (28)$$

On top of (26) and (27), we explicitly express the objective function (25a) and its gradient as (29) and (30) at the end of page 8, respectively. Those allows problem (25) to be solved

Algorithm 2: Iterative Active Beamforming Optimization by PGD with Backtracking Line Search

Input: Q, N, $\boldsymbol{h}_{\mathrm{D}}^{H}$, $\boldsymbol{H}_{\mathrm{C}}$, $\boldsymbol{\alpha}$, $\mathcal{X}$, P, σ_v^2, ρ, $\{\boldsymbol{p}_k\}_{k\in\mathcal{K}}$, $\boldsymbol{t}$, α, β, γ, ϵ
Output: $\boldsymbol{w}^{\star}$
1: Set $\boldsymbol{h}_{\mathrm{E}}^{H}(x_{m_\mathcal{K}})$, $\forall m_\mathcal{K}$ by (5)
2: $P_\mathcal{K}(x_{m_\mathcal{K}})$, $\forall m_\mathcal{K}$ by (11)
3: Initialize $r \leftarrow 0$
4: $\boldsymbol{w}^{(0)}$, $\|\boldsymbol{w}^{(0)}\|^2 \le P$
5: Get $(\sigma_{m_\mathcal{K}}^{(r)})^2$, $\forall m_\mathcal{K}$ by (7)
6: $Q^{(r)}\big(N, \frac{t_{l-1}}{\sigma_{m_\mathcal{K}}^2}, \frac{t_l}{\sigma_{m_\mathcal{K}}^2}\big)$, $\forall m_\mathcal{K}, l$ by (26)
7: $I^{(r)}(x_\mathcal{K})$ by (29)
8: $\nabla_{\boldsymbol{w}^*} Q^{(r)}\big(N, \frac{t_{l-1}}{\sigma_{m_\mathcal{K}}^2}, \frac{t_l}{\sigma_{m_\mathcal{K}}^2}\big)$, $\forall m_\mathcal{K}, l$ by (27)
9: $\nabla_{\boldsymbol{w}^*} I^{(r)}(x_\mathcal{K})$ by (30)
10: **Repeat**
11: Update $r \leftarrow r+1$
12: $\gamma^{(r)} \leftarrow \gamma$
13: $\bar{\boldsymbol{w}}^{(r)} \leftarrow \boldsymbol{w}^{(r-1)} + \gamma \nabla_{\boldsymbol{w}^*} I^{(r-1)}(x_\mathcal{K})$
14: $\boldsymbol{w}^{(r)}$ by (31)
15: Redo step 5–7
16: **While** $I^{(r)}(x_\mathcal{K}) < I^{(r-1)}(x_\mathcal{K}) + \alpha\gamma\|\nabla_{\boldsymbol{w}^*} I^{(r-1)}(x_\mathcal{K})\|^2$
17: Set $\gamma^{(r)} \leftarrow \beta\gamma^{(r)}$
18: Redo step 13–15
19: **End While**
20: Redo step 8, 9
21: **Until** $\|\boldsymbol{w}^{(r)} - \boldsymbol{w}^{(r-1)}\| \le \epsilon$

by the PGD method, where any unregulated beamforming vector $\bar{\boldsymbol{w}}$ can be projected onto the feasible domain of average transmit power constraint (21d) by

$$\boldsymbol{w} = \sqrt{P}\frac{\bar{\boldsymbol{w}}}{\max\big(\sqrt{P}, \|\bar{\boldsymbol{w}}\|\big)}. \tag{31}$$

The PGD active beamforming optimization with step size determined by backtracking line search is summarized in Algorithm 2.

C. Decision Threshold

For any given $\{\boldsymbol{p}_k\}_{k\in\mathcal{K}}$ and $\boldsymbol{w}$, problem (21) reduces to

$$\max_{\boldsymbol{t}} \quad I(x_\mathcal{K}) \tag{32a}$$

$$\text{s.t.} \quad (21e), \tag{32b}$$

which is still non-convex because variable $\boldsymbol{t}$ appears on the limits of integration (10). Fortunately, we can further simplify problem (32) as a point-to-point rate-optimal quantizer optimization for a discrete-input continuous-output memoryless channel, thanks to Remark 3 and 4.

Remark 3. *Upon successful backscatter decoding, UniScatter receiver can always re-encode node messages to recover their reflection patterns at each primary block. Therefore, backscatter decision design has no impact on the primary achievable rate, and any thresholding scheme maximizing the total backscatter mutual information* (14) *is also optimal for problem* (32).

Remark 4. *In terms of total backscatter rate, the dispersed nodes with given input distribution can be viewed as an equivalent source with augmented alphabet of backscatter symbol tuples* $\{x_{m_\mathcal{K}}\}$. *As such, the DMTMAC* (10) *is essentially a DMTC, and problem* (32) *reduces to the rate-optimal quantization design for a discrete-input continuous-output memoryless channel.*

Next, we constrain the feasible domain of problem (32) from continuous space $\mathbb{R}_+^{L+1}$ to finite candidate set (i.e., fine-grained discrete energy levels) $\mathcal{T}^{L+1}$. As shown in Fig. 5, by introducing the extra analog-to-digital conversion step, we can group adjacent high-resolution energy bins for backscatter decision regions. Thus, problem (32) is recast as

$$\max_{\boldsymbol{t}\in\mathcal{T}^{L+1}} \quad I_{\mathrm{B}}(x_\mathcal{K}; \hat{x}_\mathcal{K}), \tag{33}$$

which can be solved by existing rate-optimal Discrete Memoryless Channel (DMC) quantizer designs. For global optimal solutions, [63] proposed a Dynamic Programming (DP) method accelerated by the Shor-Moran-Aggarwal-Wilber-Klawe (SMAWK) algorithm with computational complexity $\mathcal{O}\big(L^2(\mathrm{card}(\mathcal{T})-L)\big)$, and [64] presented a traverse-then-bisect algorithm using the optimality condition of three neighbor thresholds with complexity $\mathcal{O}\big(\mathrm{card}(\mathcal{T})L\log(\mathrm{card}(\mathcal{T})L)\big)$. In

$$I(x_\mathcal{K}) = \sum_{m_\mathcal{K}} P_\mathcal{K}(x_{m_\mathcal{K}}) \Bigg(\rho\log\Big(1+\frac{|\boldsymbol{h}_{\mathrm{E}}^{H}(x_{m_\mathcal{K}})\boldsymbol{w}|^2}{\sigma_v^2}\Big) + (1-\rho)\sum_l Q\Big(N, \frac{t_{l-1}}{\sigma_{m_\mathcal{K}}^2}, \frac{t_l}{\sigma_{m_\mathcal{K}}^2}\Big)\log\frac{Q\Big(N, \frac{t_{l-1}}{\sigma_{m_\mathcal{K}}^2}, \frac{t_l}{\sigma_{m_\mathcal{K}}^2}\Big)}{\sum_{m'_\mathcal{K}} P_\mathcal{K}(x_{m'_\mathcal{K}}) Q\Big(N, \frac{t_{l-1}}{\sigma_{m'_\mathcal{K}}^2}, \frac{t_l}{\sigma_{m'_\mathcal{K}}^2}\Big)}\Bigg) \tag{29}$$

$$\begin{aligned}\nabla_{\boldsymbol{w}^*} I(x_\mathcal{K}) = \sum_{m_\mathcal{K}} P_\mathcal{K}(x_{m_\mathcal{K}}) \Bigg(&\rho\frac{\boldsymbol{h}_{\mathrm{E}}(x_{m_\mathcal{K}})\boldsymbol{h}_{\mathrm{E}}^{H}(x_{m_\mathcal{K}})\boldsymbol{w}}{\sigma_{m_\mathcal{K}}^2} + (1-\rho)\sum_l \Bigg(\log\frac{Q\Big(N, \frac{t_{l-1}}{\sigma_{m_\mathcal{K}}^2}, \frac{t_l}{\sigma_{m_\mathcal{K}}^2}\Big)}{\sum_{m'_\mathcal{K}} P_\mathcal{K}(x_{m'_\mathcal{K}}) Q\Big(N, \frac{t_{l-1}}{\sigma_{m'_\mathcal{K}}^2}, \frac{t_l}{\sigma_{m'_\mathcal{K}}^2}\Big)} + 1\Bigg) \\ &\times \nabla_{\boldsymbol{w}^*} Q\Big(N, \frac{t_{l-1}}{\sigma_{m_\mathcal{K}}^2}, \frac{t_l}{\sigma_{m_\mathcal{K}}^2}\Big) - \frac{Q\Big(N, \frac{t_{l-1}}{\sigma_{m_\mathcal{K}}^2}, \frac{t_l}{\sigma_{m_\mathcal{K}}^2}\Big)\sum_{m'_\mathcal{K}} P_\mathcal{K}(x_{m'_\mathcal{K}}) \nabla_{\boldsymbol{w}^*} Q\Big(N, \frac{t_{l-1}}{\sigma_{m'_\mathcal{K}}^2}, \frac{t_l}{\sigma_{m'_\mathcal{K}}^2}\Big)}{\sum_{m'_\mathcal{K}} P_\mathcal{K}(x_{m'_\mathcal{K}}) Q\Big(N, \frac{t_{l-1}}{\sigma_{m'_\mathcal{K}}^2}, \frac{t_l}{\sigma_{m'_\mathcal{K}}^2}\Big)}\Bigg)\end{aligned} \tag{30}$$

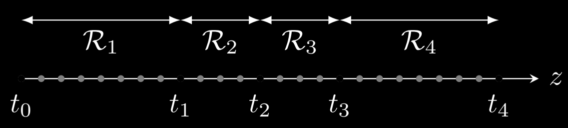

Fig. 5. The decision thresholds are selected from fine-grained discrete energy levels instead of continuous space, and each decision region consists of at least one neighbor energy bins.

Section V, both schemes will be compared with the ML thresholding scheme [65]

$$t_l^{\mathrm{ML}} = N \frac{\sigma_{l-1}^2 \sigma_l^2}{\sigma_{l-1}^2 - \sigma_l^2} \log \frac{\sigma_{l-1}^2}{\sigma_l^2}, \quad l \in \mathcal{L} \setminus \{L\}, \tag{34}$$

which is generally suboptimal for problem (32) except when all nodes are with equiprobable inputs.

V. Simulation Results

In this section, we provide numerical results to evaluate the proposed input distribution, active beamforming, and backscatter decision design for the UniScatter system in Fig. 4. We assume the AP-user distance is $10\,\mathrm{m}$, $K=2$ UniScatter nodes are randomly dropped within a disk of radius $2\,\mathrm{m}$ centered at the user, the AP is with $Q=4$ transmit antennas and an average power budget $P=36\mathrm{dBm}$, the nodes employs 4-QAM with amplitude scattering ratio $\alpha=0.5$, the user is with average noise power $\sigma_v^2=70\mathrm{dBm}$, and the symbol period ratio is $N = 20$. For all channels involved, we consider a distance-dependent path loss model

$$L(d) = L_0 \left(\frac{d_0}{d}\right)^{\gamma}, \tag{35}$$

together with a Ricean fading model

$$\boldsymbol{H} = \sqrt{\frac{\kappa}{1+\kappa}} \bar{\boldsymbol{H}} + \sqrt{\frac{1}{1+\kappa}} \tilde{\boldsymbol{H}} \tag{36}$$

where d is the transmission distance, $L_0 = -30\,\mathrm{dB}$ is the reference path loss at distance $d_0 = 1\,\mathrm{m}$, κ is the Ricean K-factor, $\bar{\boldsymbol{H}}$ is the deterministic line-of-sight component with unit-magnitude entries, and $\tilde{\boldsymbol{H}}$ is the Rayleigh fading component with entries in standard i.i.d. CSCG distribution. We choose $\gamma_{\mathrm{D}}=2.6$, $\gamma_{\mathrm{F}}=2.4$, $\gamma_{\mathrm{B}}=2$, and $\kappa_{\mathrm{D}}=\kappa_{\mathrm{F}}=\kappa_{\mathrm{B}}=5$ for direct, forward and backward links. The finite threshold domain $\mathcal{T}$ comes from b-bit uniform discretization over the critical interval defined by the confidence bounds of edge hypotheses (i.e., lower bound of $\mathcal{H}_1$ and upper bound of $\mathcal{H}_L$) with confidence level $1-\varepsilon$, where $b=8$ and $\varepsilon=2.22\times10^{-16}$. All achievable rate regions are averaged over 3000 realizations, and the parameters remain fixed unless otherwise specified.

A. Input Distribution vs. Weight

In Fig. 6, we present typical input distributions of a single UniScatter node with $M=4$ inputs under different weight ρ. Fig. 6(a) and 6(b) are obtained from i.i.d. drop and channel realizations. We note that even for $\rho=0$ (i.e., best backscatter performance), the optimal input distribution is not equiprobable like SR, and adaptive channel coding can further increase total backscatter rate based on CSI. On the other hand, the optimal

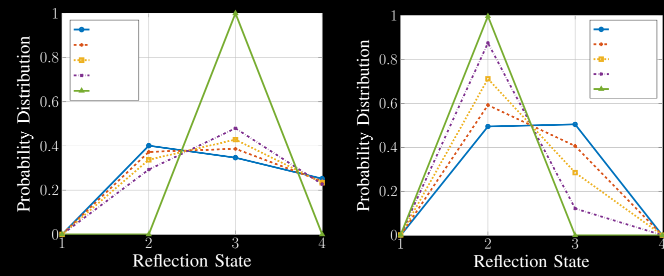

(a) Instance 1 (b) Instance 2

Fig. 6. Typical input distributions vs. weight ρ for a UniScatter node with $M=4$ inputs.

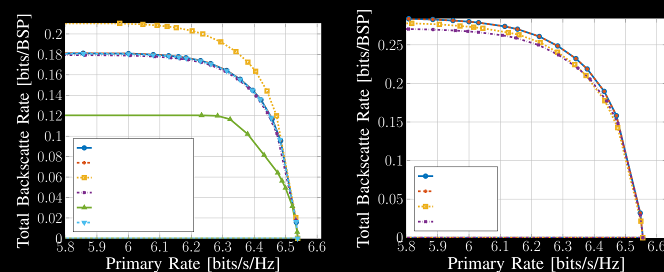

(a) Input Distribution (b) Decision Threshold

Fig. 7. Average primary-total-backscatter rate regions for different input distribution and decision threshold schemes.

input distribution becomes fully deterministic at $\rho=1$ (i.e., best primary performance), where the state maximizes equivalent primary channel (5) strength is chosen with probability 1. In this case, UniScatter node boils down to a RIS element with M discrete states. As ρ moves from 0 to 1, the optimal input distribution becomes gradually biased to one state and flexibly balances the primary-backscatter tradeoff.

B. Rate Region vs. Input, Beamforming, and Decision Schemes

Fig. 7(a) compares the achievable rate regions by following input designs.

- **Exhaustion:** K-dimensional grid search over probability simplex;
- **KKT:** results of Algorithm 1;
- **Cooperation:** backscatter cooperation/joint encoding at all UniScatter nodes, tuple input distribution/joint probability array optimization by Blahut-Arimoto algorithm [66], [67];
- **Marginalization:** marginal distributions of joint probability array;
- **Decomposition:** normalized tensors of rank-1 Canonical Polyadic (CP) decomposition of joint probability array;
- **Randomization:** Gaussian recovery from joint probability array [68].

We notice adaptive joint encoding at all nodes provides the outer bound of rate region. However, it involves arbitrarily dependent codewords, and backscatter cooperation between passive nodes is generally unaffordable. In contrast, the rate region of KKT input design in Algorithm 1 approaches that of exhaustive search, and the loss is negligible for $K = 2$. Although the randomization method [68] returns similar

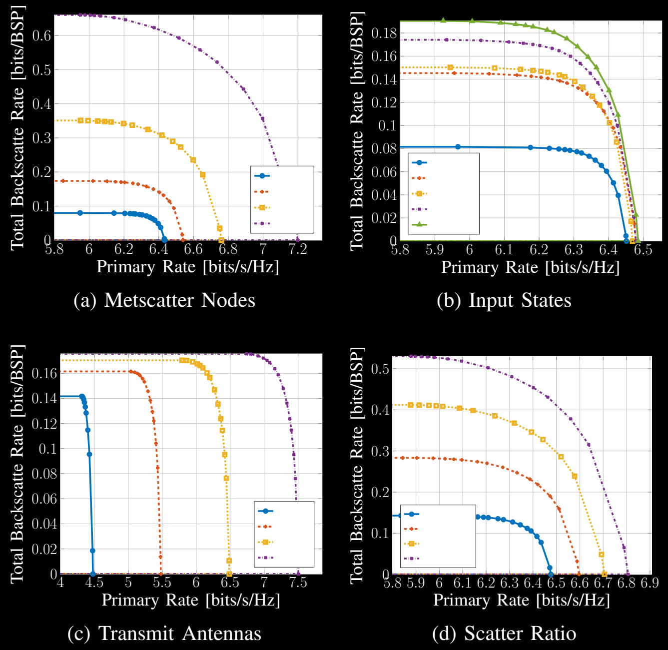

(a) Metscatter Nodes (b) Input States
(c) Transmit Antennas (d) Scatter Ratio

Fig. 8. Average primary-total-backscatter rate regions.

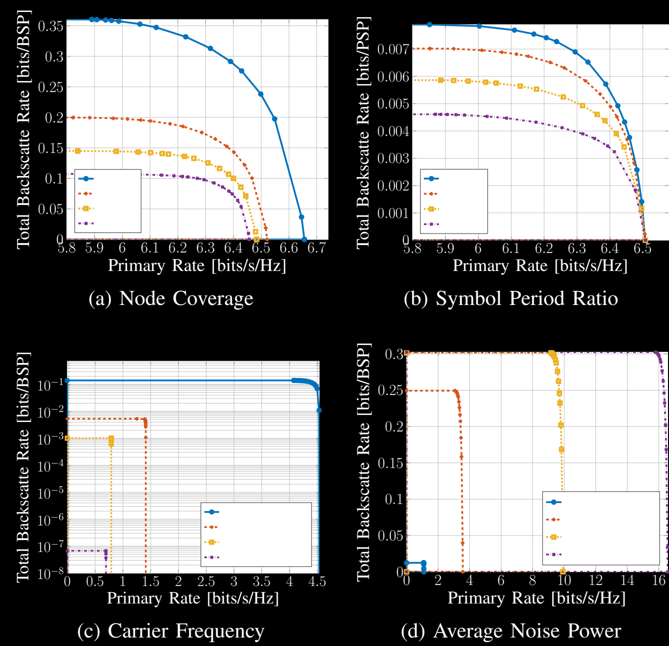

(a) Node Coverage (b) Symbol Period Ratio
(c) Carrier Frequency (d) Average Noise Power

Fig. 9. Average primary-total-backscatter rate regions.

rate region, it requires solving $K+1$ linear programming problems before applying Gaussian recovery. The marginal distribution is slightly worse than KKT despite having the same computational complexity, while the approximation from CP decomposition is unsatisfying.

Fig. 7(b) compares the achievable rate region by following threshold schemes.

- **DP:** sequential quantizer grouping by dynamic programming [63];
- **SMAWK:** above accelerated by SMAWK algorithm;
- **Bisection:** sequential bisection threshold design [64];
- **ML:** maximum likelihood decision (34) [65].

We observe that input distribution-adaptive threshold designs achieve higher total backscatter rate than ML. This is because the decision regions can be flexibly adjusted to enhance the capacity of DMTMAC (10). For example, the tuples with negligible input probability should have narrower decision regions than those frequently employed, in order to improve detection performance. It emphasizes the importance of joint input distribution and decision region design.

C. Rate Region vs. System Configuration

We present in 8 the impact of UniScatter nodes, input states, transmit antennas and scatter ratio on the achievable rate region. For the specified scenario, Fig. 8(a) shows the total backscatter rate almost scales proportionally with the number of UniScatter nodes, and the decrease of individual backscatter rate is unobvious. Besides, we conclude from 8(b) that increasing the reflection states has a marginal effect on both primary and backscatter rates. Those two facts motivates the use of numerous elementary/uncomplicated backscatter nodes, instead of high-order transponders or programmable high-resolution surfaces. Figs. 8(c) and 8(d) also prove increasing transmit antennas or scatter ratio can improve both primary and backscatter performance.

Fig. 9(a) shows the tradeoff between coverage disk radius r and achievable rate region. When nodes are far from the user, both primary and backscatter rates decrease due to the product pass loss of forward and backward channels. Under the assumption of ideal backscatter decoding and re-encoding, Fig. 9(b) suggests using lower symbol period ratio N can boost total backscatter rate per primary symbol. However, it requires more frequent detection and re-encoding at the user to maintain the primary rate. When N becomes sufficiently large, total backscatter rate approaches 0 and UniScatter nodes boil down to conventional RIS elements with fixed reflection pattern during whole channel block. In Fig. 9(c), we observe that passive UniScatter nodes achieve higher backscatter rate at lower carrier frequency because of preferable propagation loss. Finally, 9(d) prove the performance of energy detection is robust for a wide range of noise power.

VI. Conclusion

This paper introduced UniScatter that adapts input distribution of passive backscatter nodes to simultaneously transmit and assist over existing wireless systems. Starting from backscatter principles, we showed how UniScatter nodes bridges and generalizes parasitic source of SR and reflecting element of RIS via smart input design. An application scenario was considered where multiple UniScatter nodes ride over a point-to-point transmission to simultaneously encode self message and perform passive beamforming. To characterize achievable primary-backscatter rate region, we proposed a BCD algorithm that evaluates KKT input distribution in closed form, optimizes active beamforming by PGD, and refines decision regions by existing methods. Numerical results demonstrated the advantage of adaptive node input distribution design for both primary and backscatter subsystems.

One particular interesting question is how to design UniScatter node and receiver in a multi-user system. If one node can contribute to and be decoded by multiple users, its input distribution may be further adjusted to mimic multi-beam gain of dynamic beamforming [69].

Appendix

A. Proof of Proposition 1

Denote the Lagrange multipliers associated with (21b) and (21c) as $\{\nu_k\}_{k\in\mathcal{K}}$ and $\{\lambda_{k,m_k}\}_{k\in\mathcal{K},m_k\in\mathcal{M}}$, respectively. The Lagrangian function of problem (22) is

$$-I(x_{\mathcal{K}})+\sum_k \nu_k\left(\sum_{m_k}P_k(x_{m_k})-1\right)-\sum_k\sum_{m_k}\lambda_{k,m_k}P_k(x_{m_k}) \tag{37}$$

and the KKT conditions are, $\forall k,m_k$,

$$-\nabla_{P_k^\star(x_{m_k})}I^\star(x_{\mathcal{K}})+\nu_k^\star-\lambda_{k,m_k}^\star=0, \tag{38a}$$

$$\lambda_{k,m_k}^\star=0,\quad P_k^\star(x_{m_k})>0, \tag{38b}$$

$$\lambda_{k,m_k}^\star\geq 0,\quad P_k^\star(x_{m_k})=0, \tag{38c}$$

where directional derivative is explicitly written as

$$\nabla_{P_k^\star(x_{m_k})}I^\star(x_{\mathcal{K}})=I_k^\star(x_{m_k})-(1-\rho). \tag{39}$$

Combining (38) and (39), we have

$$I_k^\star(x_{m_k})=\nu_k^\star+(1-\rho),\quad P_k^\star(x_{m_k})>0, \tag{40a}$$

$$I_k^\star(x_{m_k})\leq\nu_k^\star+(1-\rho),\quad P_k^\star(x_{m_k})=0, \tag{40b}$$

such that

$$\sum_{m_k}P_k^\star(x_{m_k})I_k^\star(x_{m_k})=\nu_k^\star+(1-\rho). \tag{41}$$

On the other hand, by definition (19) we have

$$\sum_{m_k}P_k^\star(x_{m_k})I_k^\star(x_{m_k})=I^\star(x_{\mathcal{K}}), \tag{42}$$

where the right-hand side is irrelevant to k. (40), (41), and (42) together complete the proof.

B. Proof of Proposition 2

We first prove sequence (24) is non-decreasing in weighted sum mutual information. Let $P_{\mathcal{K}}(x_{m_{\mathcal{K}}})=\prod_{q\in\mathcal{K}}P_q(x_{m_q})$ and $P'_{\mathcal{K}}(x_{m_{\mathcal{K}}})=P'_k(x_{m_k})\prod_{q\in\mathcal{K}\setminus\{k\}}P_q(x_{m_q})$ be two probability distributions with potentially different marginal for tag k at state m_k, and define an intermediate function $J\big(P_{\mathcal{K}}(x_{m_{\mathcal{K}}}),P'_{\mathcal{K}}(x_{m_{\mathcal{K}}})\big)$ as (43) at the end of page 11. It is straightforward to verify $J\big(P_{\mathcal{K}}(x_{m_{\mathcal{K}}}),P_{\mathcal{K}}(x_{m_{\mathcal{K}}})\big)=I(x_{\mathcal{K}})$ and $J\big(P_{\mathcal{K}}(x_{m_{\mathcal{K}}}),P'_{\mathcal{K}}(x_{m_{\mathcal{K}}})\big)$ is a concave function for a fixed $P'_{\mathcal{K}}(x_{m_{\mathcal{K}}})$. Setting $\nabla_{P_k^\star(x_{m_k})}J\big(P_{\mathcal{K}}(x_{m_{\mathcal{K}}}),P'_{\mathcal{K}}(x_{m_{\mathcal{K}}})\big)=0$, we have

$$S'_k(x_{m_k})-S'_k(x_{i_k})+(1-\rho)\log\frac{P_k(x_{i_k})}{P_k^\star(x_{m_k})}=0, \tag{44}$$

where $i_k\neq m_k$ is the reference state and

$$S'_k(x_{m_k})\triangleq I'_k(x_{m_k})+(1-\rho)\sum_{m_{\mathcal{K}\setminus\{k\}}}P_{\mathcal{K}\setminus\{k\}}(x_{m_{\mathcal{K}\setminus\{k\}}}) \times\sum_{m'_{\mathcal{K}}}P(\hat{x}_{m'_{\mathcal{K}}}|x_{m_{\mathcal{K}}})\log P'_{\mathcal{K}}(x_{m_{\mathcal{K}}}). \tag{45}$$

Evidently, $\forall m_k\neq i_k$, (44) boils down to

$$P_k^\star(x_{m_k})=\frac{P'_k(x_{m_k})\exp\Big(\frac{\rho}{1-\rho}I'_k(x_{m_k})\Big)}{\sum_{m'_k}P'_k(x_{m'_k})\exp\Big(\frac{\rho}{1-\rho}I'_k(x_{m'_k})\Big)}. \tag{46}$$

Since $P_k(x_{i_k})=1-\sum_{m_k\neq i_k}P_k^\star(x_{m_k})$ has exactly the same form as (46), the choice of reference state i_k does not matter and (46) is indeed optimal $\forall m_k\in\mathcal{M}$. That is, for a fixed $P'_{\mathcal{K}}(x_{m_{\mathcal{K}}})$, choosing $P_k(x_{m_k})$ by (46) ensures

$$J\big(P_{\mathcal{K}}(x_{m_{\mathcal{K}}}),P'_{\mathcal{K}}(x_{m_{\mathcal{K}}})\big)\geq I'(x_{\mathcal{K}}). \tag{47}$$

On the other hand, we also have

$$\begin{aligned}
\Delta&\triangleq I(x_{\mathcal{K}})-J\big(P_{\mathcal{K}}(x_{m_{\mathcal{K}}}),P'_{\mathcal{K}}(x_{m_{\mathcal{K}}})\big) &\text{(48a)}\\
&=(1-\rho)\sum_{m_k}\frac{P'_k(x_{m_k})f'_k(x_{m_k})}{\sum_{m'_k}P'_k(x_{m'_k})f'_k(x_{m'_k})}\sum_{m''_{\mathcal{K}}}P(\hat{x}_{m''_{\mathcal{K}}}|x_{m_k})\\
&\quad\times\log\frac{\sum_{m'_k}P'_k(x_{m'_k})P(\hat{x}_{m''_{\mathcal{K}}}|x_{m'_k})f'_k(x_{m_k})}{\sum_{m'_k}P'_k(x_{m'_k})P(\hat{x}_{m''_{\mathcal{K}}}|x_{m'_k})f'_k(x_{m'_k})} &\text{(48b)}\\
&\geq(1-\rho)\sum_{m_k}\frac{P'_k(x_{m_k})f'_k(x_{m_k})}{\sum_{m'_k}P'_k(x_{m'_k})f'_k(x_{m'_k})}\sum_{m''_{\mathcal{K}}}P(\hat{x}_{m''_{\mathcal{K}}}|x_{m_k})\\
&\quad\times\left(1-\frac{\sum_{m'_k}P'_k(x_{m'_k})P(\hat{x}_{m''_{\mathcal{K}}}|x_{m'_k})f'_k(x_{m'_k})}{\sum_{m'_k}P'_k(x_{m'_k})P(\hat{x}_{m''_{\mathcal{K}}}|x_{m'_k})f'_k(x_{m_k})}\right) &\text{(48c)}\\
&=0, &\text{(48d)}
\end{aligned}$$

where $f'_k(x_{m_k})\triangleq\exp\big(\frac{\rho}{1-\rho}I'_k(x_{m_k})\big)$ and the equality holds if and only if (46) converges. (47) and (48) together imply $I(x_{\mathcal{K}})\geq I'(x_{\mathcal{K}})$. Since mutual information is bounded above, we conclude the sequence (24) is non-decreasing and convergent in mutual information.

Next, we prove any converging point of sequence (24), denoted as $P_k^\star(x_{m_k})$, fulfills KKT conditions (23). To see this, let

$$D_k^{(r)}(x_{m_k})\triangleq\frac{P_k^{(r+1)}(x_{m_k})}{P_k^{(r)}(x_{m_k})}=\frac{f_k^{(r)}(x_{m_k})}{\sum_{m'_k}P_k^{(r)}(x_{m'_k})f_k^{(r)}(x_{m'_k})}. \tag{49}$$

As sequence (24) is convergent, any state with $P_k^\star(x_{m_k})>0$ need to satisfy $D_k^\star(x_{m_k})\triangleq\lim_{r\to\infty}D_k^{(r)}(x_{m_k})=1$, namely

$$I_k^\star(x_{m_k})=\frac{1-\rho}{\rho}\log\sum_{m'_k}P_k^\star(x_{m'_k})f_k^\star(x_{m'_k}), \tag{50}$$

which is reminiscent of (40a) and (23a). That is, given $P_k^{(0)}(x_{m_k})>0$, any converging point with $P_k^\star(x_{m_k})>0$ must

$$J\big(P_{\mathcal{K}}(x_{m_{\mathcal{K}}}),P'_{\mathcal{K}}(x_{m_{\mathcal{K}}})\big)\triangleq\sum_{m_{\mathcal{K}}}P_{\mathcal{K}}(x_{m_{\mathcal{K}}})\left(\rho\log\Big(1+\frac{|\boldsymbol{h}_{\mathrm{E}}^H(x_{m_{\mathcal{K}}})\boldsymbol{w}|^2}{\sigma_v^2}\Big)+(1-\rho)\sum_{m'_{\mathcal{K}}}P(\hat{x}_{m'_{\mathcal{K}}}|x_{m_{\mathcal{K}}})\log\frac{P(\hat{x}_{m'_{\mathcal{K}}}|x_{m_{\mathcal{K}}})P'_{\mathcal{K}}(x_{m_{\mathcal{K}}})}{P'_{\mathcal{K}}(\hat{x}_{m'_{\mathcal{K}}})P_{\mathcal{K}}(x_{m_{\mathcal{K}}})}\right). \tag{43}$$

satisfy (23a). On the other hand, we assume $P_k^\star(x_{m_k})$ does not satisfy (23b), such that for any state with $P_k^\star(x_{m_k})=0$,

$$I_k^\star(x_{m_k})>I^\star(x_{\mathcal{K}})=\sum_{m_k'}P_k^\star(x_{m_k'})I_k^\star(x_{m_k'}), \tag{51}$$

where the equality inherits from (20). Since the exponential function is monotonically increasing, we have $f_k^\star(x_{m_k})>\sum_{m_k'}P_k^\star(x_{m_k'})f_k^\star(x_{m_k'})$ and $D_k^\star(x_{m_k})>1$. Considering $P_k^{(0)}(x_{m_k})>0$ and $P_k^\star(x_{m_k})=0$, it contradicts with

$$P_k^{(r)}(x_{m_k})=P_k^{(0)}(x_{m_k})\prod_{n=1}^{r}D_k^{(n)}(x_{m_k}). \tag{52}$$

That is, given $P_k^{(0)}(x_{m_k})>0$, any converging point with $P_k^\star(x_{m_k})=0$ must satisfy (23b). The proof is thus completed.

References

[1] C. Boyer and S. Roy, "Backscatter communication and rfid: Coding, energy, and mimo analysis," *IEEE Transactions on Communications*, vol. 62, pp. 770–785, 3 2014. [Online]. Available: http://ieeexplore.ieee.org/document/6685977/

[2] D. Dobkin, *The RF in RFID: Passive UHF RFID in Practice*. Newnes, 11 2012. [Online]. Available: https://www.elsevier.com/books/the-rf-in-rfid/dobkin/978-0-12-394583-9

[3] J. Landt, "The history of rfid," *IEEE Potentials*, vol. 24, pp. 8–11, 10 2005.

[4] G. Vannucci, A. Bletsas, and D. Leigh, "A software-defined radio system for backscatter sensor networks," *IEEE Transactions on Wireless Communications*, vol. 7, pp. 2170–2179, 6 2008. [Online]. Available: http://ieeexplore.ieee.org/document/4543069/

[5] S. D. Assimonis, S. N. Daskalakis, and A. Bletsas, "Sensitive and efficient rf harvesting supply for batteryless backscatter sensor networks," *IEEE Transactions on Microwave Theory and Techniques*, vol. 64, pp. 1327–1338, 4 2016.

[6] V. Liu, A. Parks, V. Talla, S. Gollakota, D. Wetherall, and J. R. Smith, "Ambient backscatter: Wireless communication out of thin air," *ACM SIGCOMM Computer Communication Review*, vol. 43, pp. 39–50, 9 2013. [Online]. Available: https://dl.acm.org/doi/10.1145/2534169.2486015

[7] G. Yang, Q. Zhang, and Y.-C. Liang, "Cooperative ambient backscatter communications for green internet-of-things," *IEEE Internet of Things Journal*, vol. 5, pp. 1116–1130, 4 2018. [Online]. Available: https://ieeexplore.ieee.org/document/8274950/

[8] Y.-C. Liang, Q. Zhang, E. G. Larsson, and G. Y. Li, "Symbiotic radio: Cognitive backscattering communications for future wireless networks," *IEEE Transactions on Cognitive Communications and Networking*, vol. 6, pp. 1242–1255, 12 2020. [Online]. Available: https://ieeexplore.ieee.org/document/9193946/

[9] H. Guo, Y.-C. Liang, R. Long, and Q. Zhang, "Cooperative ambient backscatter system: A symbiotic radio paradigm for passive iot," *IEEE Wireless Communications Letters*, vol. 8, pp. 1191–1194, 8 2019. [Online]. Available: https://ieeexplore.ieee.org/document/8692391/

[10] H. Ding, D. B. da Costa, and J. Ge, "Outage analysis for cooperative ambient backscatter systems," *IEEE Wireless Communications Letters*, vol. 9, pp. 601–605, 5 2020. [Online]. Available: https://ieeexplore.ieee.org/document/8941106/

[11] Q. Zhang, Y.-C. Liang, H.-C. Yang, and H. V. Poor, "Mutualistic mechanism in symbiotic radios: When can the primary and secondary transmissions be mutually beneficial?" *IEEE Transactions on Wireless Communications*, vol. 1276, pp. 1–1, 2022. [Online]. Available: https://ieeexplore.ieee.org/document/9751388/

[12] R. Long, Y.-C. Liang, H. Guo, G. Yang, and R. Zhang, "Symbiotic radio: A new communication paradigm for passive internet of things," *IEEE Internet of Things Journal*, vol. 7, pp. 1350–1363, 2 2020. [Online]. Available: https://ieeexplore.ieee.org/document/8907447/

[13] S. Zhou, W. Xu, K. Wang, C. Pan, M.-S. Alouini, and A. Nallanathan, "Ergodic rate analysis of cooperative ambient backscatter communication," *IEEE Wireless Communications Letters*, vol. 8, pp. 1679–1682, 12 2019. [Online]. Available: https://ieeexplore.ieee.org/document/8807353/

[14] T. Wu, M. Jiang, Q. Zhang, Q. Li, and J. Qin, "Beamforming design in multiple-input-multiple-output symbiotic radio backscatter systems," *IEEE Communications Letters*, vol. 25, pp. 1949–1953, 6 2021. [Online]. Available: https://ieeexplore.ieee.org/document/9358202/

[15] J. Xu, Z. Dai, and Y. Zeng, "Enabling full mutualism for symbiotic radio with massive backscatter devices," *arXiv:2106.05789*, 6 2021. [Online]. Available: http://arxiv.org/abs/2106.05789

[16] H. Yang, Y. Ye, K. Liang, and X. Chu, "Energy efficiency maximization for symbiotic radio networks with multiple backscatter devices," *IEEE Open Journal of the Communications Society*, vol. 2, pp. 1431–1444, 2021. [Online]. Available: https://ieeexplore.ieee.org/document/9461158/

[17] S. Han, Y.-C. Liang, and G. Sun, "The design and optimization of random code assisted multi-bd symbiotic radio system," *IEEE Transactions on Wireless Communications*, vol. 20, pp. 5159–5170, 8 2021. [Online]. Available: https://ieeexplore.ieee.org/document/9382925/

[18] G. Vougioukas and A. Bletsas, "Switching frequency techniques for universal ambient backscatter networking," *IEEE Journal on Selected Areas in Communications*, vol. 37, pp. 464–477, 2 2019. [Online]. Available: https://ieeexplore.ieee.org/document/8474355/

[19] Q. Wu, S. Zhang, B. Zheng, C. You, and R. Zhang, "Intelligent reflecting surface-aided wireless communications: A tutorial," *IEEE Transactions on Communications*, vol. 69, pp. 3313–3351, 5 2021. [Online]. Available: https://ieeexplore.ieee.org/document/9326394/

[20] Q. Wu and R. Zhang, "Intelligent reflecting surface enhanced wireless network: Joint active and passive beamforming design," vol. 18. IEEE, 12 2018, pp. 1–6. [Online]. Available: https://ieeexplore.ieee.org/document/8647620/

[21] S. Zhang and R. Zhang, "Capacity characterization for intelligent reflecting surface aided mimo communication," *IEEE Journal on Selected Areas in Communications*, vol. 38, pp. 1823–1838, 8 2020. [Online]. Available: https://ieeexplore.ieee.org/document/9110912/

[22] S. Lin, B. Zheng, F. Chen, and R. Zhang, "Intelligent reflecting surface-aided spectrum sensing for cognitive radio," *IEEE Wireless Communications Letters*, vol. 11, pp. 928–932, 5 2022.

[23] Y. Liu, Y. Zhang, X. Zhao, S. Geng, P. Qin, and Z. Zhou, "Dynamic-controlled ris assisted multi-user miso downlink system: Joint beamforming design," *IEEE Transactions on Green Communications and Networking*, vol. 6, pp. 1069–1081, 6 2022.

[24] Z. Feng, B. Clerckx, and Y. Zhao, "Waveform and beamforming design for intelligent reflecting surface aided wireless power transfer: Single-user and multi-user solutions," *IEEE Transactions on Wireless Communications*, 2022.

[25] Y. Zhao, B. Clerckx, and Z. Feng, "Irs-aided swipt: Joint waveform, active and passive beamforming design under nonlinear harvester model," *IEEE Transactions on Communications*, vol. 70, pp. 1345–1359, 2022.

[26] Q. Wu, X. Zhou, and R. Schober, "Irs-assisted wireless powered noma: Do we really need different phase shifts in dl and ul?" *arXiv:2102.08739*, vol. 10, pp. 1493–1497, 7 2021. [Online]. Available: https://ieeexplore.ieee.org/document/9400380/

[27] Q. Wu, X. Zhou, W. Chen, J. Li, and X. Zhang, "Irs-aided wpcns: A new optimization framework for dynamic irs beamforming," *IEEE Transactions on Wireless Communications*, pp. 1–1, 12 2021.

[28] M. Hua and Q. Wu, "Joint dynamic passive beamforming and resource allocation for irs-aided full-duplex wpcn," *IEEE Transactions on Wireless Communications*, pp. 1–1, 12 2021.

[29] R. Karasik, O. Simeone, M. D. Renzo, and S. S. Shitz, "Beyond max-snr: Joint encoding for reconfigurable intelligent surfaces," vol. 2020-June. IEEE, 6 2020, pp. 2965–2970. [Online]. Available: https://ieeexplore.ieee.org/document/9174060/

[30] R. Liu, H. Li, M. Li, and Q. Liu, "Symbol-level precoding design for intelligent reflecting surface assisted multi-user mimo systems." IEEE, 10 2019, pp. 1–6. [Online]. Available: https://ieeexplore.ieee.org/document/8928065/

[31] A. Bereyhi, V. Jamali, R. R. Muller, A. M. Tulino, G. Fischer, and R. Schober, "A single-rf architecture for multiuser massive mimo via reflecting surfaces." IEEE, 5 2020, pp. 8688–8692. [Online]. Available: https://ieeexplore.ieee.org/document/9052989/

[32] X. Xu, Y.-C. Liang, G. Yang, and L. Zhao, "Reconfigurable intelligent surface empowered symbiotic radio over broadcasting signals," vol. 2020-Janua. IEEE, 12 2020, pp. 1–6. [Online]. Available: https://ieeexplore.ieee.org/document/9348236/

[33] Q. Zhang, Y.-C. Liang, and H. V. Poor, "Reconfigurable intelligent surface assisted mimo symbiotic radio networks," *IEEE Transactions on Communications*, vol. 69, pp. 4832–4846, 7 2021. [Online]. Available: https://ieeexplore.ieee.org/document/9391685/

[34] J. Hu, Y. C. Liang, and Y. Pei, "Reconfigurable intelligent surface enhanced multi-user miso symbiotic radio system," *IEEE Transactions on Communications*, vol. 69, pp. 2359–2371, 4 2021.

[35] M. Hua, Q. Wu, L. Yang, R. Schober, and H. V. Poor, "A novel wireless communication paradigm for intelligent reflecting surface based symbiotic

radio systems," *IEEE Transactions on Signal Processing*, vol. 70, pp. 550–565, 4 2022. [Online]. Available: http://arxiv.org/abs/2104.09161https://ieeexplore.ieee.org/document/9652042/

[36] E. Basar, "Reconfigurable intelligent surface-based index modulation: A new beyond mimo paradigm for 6g," *IEEE Transactions on Communications*, vol. 68, pp. 3187–3196, 5 2020. [Online]. Available: https://ieeexplore.ieee.org/document/8981888/

[37] T. Ma, Y. Xiao, X. Lei, P. Yang, X. Lei, and O. A. Dobre, "Large intelligent surface assisted wireless communications with spatial modulation and antenna selection," *IEEE Journal on Selected Areas in Communications*, vol. 38, pp. 2562–2574, 11 2020. [Online]. Available: https://ieeexplore.ieee.org/document/9133588/

[38] J. Yuan, M. Wen, Q. Li, E. Basar, G. C. Alexandropoulos, and G. Chen, "Receive quadrature reflecting modulation for ris-empowered wireless communications," *IEEE Transactions on Vehicular Technology*, vol. 70, pp. 5121–5125, 5 2021. [Online]. Available: https://ieeexplore.ieee.org/document/9405433/

[39] S. Hu, C. Liu, Z. Wei, Y. Cai, D. W. K. Ng, and J. Yuan, "Beamforming design for intelligent reflecting surface-enhanced symbiotic radio systems," *arxiv:2110.10316*, 10 2021. [Online]. Available: http://arxiv.org/abs/2110.10316

[40] Y. C. Liang, Q. Zhang, J. Wang, R. Long, H. Zhou, and G. Yang, "Backscatter communication assisted by reconfigurable intelligent surfaces," *Proceedings of the IEEE*, 2022.

[41] S. J. Thomas, E. Wheeler, J. Teizer, and M. S. Reynolds, "Quadrature amplitude modulated backscatter in passive and semipassive uhf rfid systems," *IEEE Transactions on Microwave Theory and Techniques*, vol. 60, pp. 1175–1182, 4 2012. [Online]. Available: http://ieeexplore.ieee.org/document/6153042/

[42] R. Hansen, "Relationships between antennas as scatterers and as radiators," *Proceedings of the IEEE*, vol. 77, pp. 659–662, 5 1989. [Online]. Available: http://ieeexplore.ieee.org/document/32056/

[43] Q. Wu and R. Zhang, "Towards smart and reconfigurable environment: Intelligent reflecting surface aided wireless network," *IEEE Communications Magazine*, vol. 58, pp. 106–112, 1 2020. [Online]. Available: https://ieeexplore.ieee.org/document/8910627/

[44] J. Zhou, P. Zhang, J. Han, L. Li, and Y. Huang, "Metamaterials and metasurfaces for wireless power transfer and energy harvesting," *Proceedings of the IEEE*, vol. 110, pp. 31–55, 1 2022.

[45] Y. Huang, *Antennas: From Theory to Practice*. Wiley, 9 2021.

[46] A. Singh, M. Andrello, N. Thawdar, and J. M. Jornet, "Design and operation of a graphene-based plasmonic nano-antenna array for communication in the terahertz band," *IEEE Journal on Selected Areas in Communications*, vol. 38, pp. 2104–2117, 9 2020.

[47] F. Costa and M. Borgese, "Electromagnetic model of reflective intelligent surfaces," *IEEE Open Journal of the Communications Society*, vol. 2, pp. 1577–1589, 2021.

[48] M. E. Bialkowski and K. H. Sayidmarie, "Investigations into phase characteristics of a single-layer reflectarray employing patch or ring elements of variable size," *IEEE Transactions on Antennas and Propagation*, vol. 56, pp. 3366–3372, 2008.

[49] B. Clerckx, R. Zhang, R. Schober, D. W. K. Ng, D. I. Kim, and H. V. Poor, "Fundamentals of wireless information and power transfer: From rf energy harvester models to signal and system designs," *IEEE Journal on Selected Areas in Communications*, vol. 37, pp. 4–33, 1 2019. [Online]. Available: https://ieeexplore.ieee.org/document/8476597/

[50] J. Kim and B. Clerckx, "Wireless information and power transfer for iot: Pulse position modulation, integrated receiver, and experimental validation," *arXiv:2104.08404*, pp. 1–15, 4 2021. [Online]. Available: http://arxiv.org/abs/2104.08404

[51] D. Bharadia, K. R. Joshi, M. Kotaru, and S. Katti, "Backfi: High throughput wifi backscatter," vol. 45. ACM, 8 2015, pp. 283–296. [Online]. Available: https://dl.acm.org/doi/10.1145/2785956.2787490

[52] G. Yang, C. K. Ho, and Y. L. Guan, "Multi-antenna wireless energy transfer for backscatter communication systems," *IEEE Journal on Selected Areas in Communications*, vol. 33, pp. 2974–2987, 12 2015. [Online]. Available: http://ieeexplore.ieee.org/document/7274644/

[53] H. Guo, Q. Zhang, S. Xiao, and Y.-C. Liang, "Exploiting multiple antennas for cognitive ambient backscatter communication," *IEEE Internet of Things Journal*, vol. 6, pp. 765–775, 2 2019. [Online]. Available: https://ieeexplore.ieee.org/document/8411483/

[54] M. Jin, Y. He, C. Jiang, and Y. Liu, "Parallel backscatter: Channel estimation and beyond," *IEEE/ACM Transactions on Networking*, vol. 29, pp. 1128–1140, 6 2021. [Online]. Available: https://ieeexplore.ieee.org/document/9377568/

[55] Y. Huang, A. Alieldin, and C. Song, "Equivalent circuits and analysis of a generalized antenna system," *IEEE Antennas and Propagation Magazine*, vol. 63, pp. 53–62, 4 2021. [Online]. Available: https://ieeexplore.ieee.org/document/9392844/

[56] J. Qian, Y. Zhu, C. He, F. Gao, and S. Jin, "Achievable rate and capacity analysis for ambient backscatter communications," *IEEE Transactions on Communications*, vol. 67, pp. 6299–6310, 9 2019. [Online]. Available: https://ieeexplore.ieee.org/document/8721108/

[57] T. Nguyen and T. Nguyen, "Capacity achieving quantizer design for binary channels," *IEEE Communications Letters*, vol. 25, pp. 759–763, 3 2021. [Online]. Available: https://ieeexplore.ieee.org/document/9247251/

[58] T. Nguyen, Y.-J. Chu, and T. Nguyen, "On the capacities of discrete memoryless thresholding channels," vol. 2018-June. IEEE, 6 2018, pp. 1–5. [Online]. Available: https://ieeexplore.ieee.org/document/8417506/

[59] T. Nguyen and T. Nguyen, "Optimal quantizer structure for maximizing mutual information under constraints," *IEEE Transactions on Communications*, vol. 69, pp. 7406–7413, 11 2021. [Online]. Available: https://ieeexplore.ieee.org/document/9530430/

[60] M. Rezaeian and A. Grant, "Computation of total capacity for discrete memoryless multiple-access channels," *IEEE Transactions on Information Theory*, vol. 50, pp. 2779–2784, 11 2004. [Online]. Available: http://ieeexplore.ieee.org/document/1347364/

[61] J. Buhler and G. Wunder, "A note on capacity computation for the discrete multiple access channel," *IEEE Transactions on Information Theory*, vol. 57, pp. 1906–1910, 4 2011. [Online]. Available: https://ieeexplore.ieee.org/document/5730559/

[62] G. J. O. Jameson, "The incomplete gamma functions," *The Mathematical Gazette*, vol. 100, pp. 298–306, 7 2016. [Online]. Available: https://www.cambridge.org/core/product/identifier/S002555721600067X/type/journal_article

[63] X. He, K. Cai, W. Song, and Z. Mei, "Dynamic programming for sequential deterministic quantization of discrete memoryless channels," *IEEE Transactions on Communications*, vol. 69, pp. 3638–3651, 6 2021. [Online]. Available: https://ieeexplore.ieee.org/document/9366549/

[64] T. Nguyen and T. Nguyen, "On thresholding quantizer design for mutual information maximization: Optimal structures and algorithms," vol. 2020-May. IEEE, 5 2020, pp. 1–5. [Online]. Available: https://ieeexplore.ieee.org/document/9128966/

[65] J. Qian, A. N. Parks, J. R. Smith, F. Gao, and S. Jin, "Iot communications with m-psk modulated ambient backscatter: Algorithm, analysis, and implementation," *IEEE Internet of Things Journal*, vol. 6, pp. 844–855, 2 2019. [Online]. Available: https://ieeexplore.ieee.org/document/8423609/

[66] S. Arimoto, "An algorithm for computing the capacity of arbitrary discrete memoryless channels," *IEEE Transactions on Information Theory*, vol. 18, pp. 14–20, 1 1972. [Online]. Available: http://ieeexplore.ieee.org/document/1054753/

[67] R. E. Blahut, "Computation of channel capacity and rate-distortion functions," *IEEE Transactions on Information Theory*, vol. 18, pp. 460–473, 7 1972. [Online]. Available: http://ieeexplore.ieee.org/document/1054855/

[68] E. Calvo, D. P. Palomar, J. R. Fonollosa, and J. Vidal, "On the computation of the capacity region of the discrete mac," *IEEE Transactions on Communications*, vol. 58, pp. 3512–3525, 12 2010. [Online]. Available: http://ieeexplore.ieee.org/document/5590317/

[69] C. Qiu, Q. Wu, M. Hua, X. guan, and Y. Wu, "Achieving multi-beam gain in intelligent reflecting surface assisted wireless energy transfer," *arXiv:2205.08893*, 5 2022. [Online]. Available: http://arxiv.org/abs/2205.08893